Supplemental Material for
"Quantum simulation of topological zero modes on a 41-qubit superconducting processor"

Yun-Hao Shi,[1,2,3,*] Yu Liu,[1,2,*] Yu-Ran Zhang,[4,5,6,*] Zhongcheng Xiang,[1,2,*] Kaixuan Huang,[3,1] Tao Liu,[4]
Yong-Yi Wang,[1,2] Jia-Chi Zhang,[1,2] Cheng-Lin Deng,[1,2] Gui-Han Liang,[1,2] Zheng-Yang Mei,[1,2] Hao Li,[1]
Tian-Ming Li,[1,2] Wei-Guo Ma,[1,2] Hao-Tian Liu,[1,2] Chi-Tong Chen,[1,2] Tong Liu,[1,2] Ye Tian,[1] Xiaohui Song,[1]
S. P. Zhao,[1,2,7] Kai Xu,[1,2,3,7,8,†] Dongning Zheng,[1,2,7,8,‡] Franco Nori,[5,6,9,§] and Heng Fan[1,2,3,7,8,10,¶]

[1]*Institute of Physics, Chinese Academy of Sciences, Beijing 100190, China*
[2]*School of Physical Sciences, University of Chinese Academy of Sciences, Beijing 100049, China*
[3]*Beijing Academy of Quantum Information Sciences, Beijing 100193, China*
[4]*School of Physics and Optoelectronics, South China University of Technology, Guangzhou 510640, China*
[5]*Theoretical Quantum Physics Laboratory, Cluster for Pioneering Research, RIKEN, Wako-shi, Saitama 351-0198, Japan*
[6]*Center for Quantum Computing, RIKEN, Wako-shi, Saitama 351-0198, Japan*
[7]*Songshan Lake Materials Laboratory, Dongguan, Guangdong 523808, China*
[8]*CAS Center for Excellence in Topological Quantum Computation, UCAS, Beijing 100049, China*
[9]*Physics Department, University of Michigan, Ann Arbor, Michigan 48109-1040, USA*
[10]*Hefei National Laboratory, Hefei 230088, China*

CONTENTS

---

* These authors contributed equally to this work.
† kaixu@iphy.ac.cn
‡ dzheng@iphy.ac.cn
§ fnori@riken.jp
¶ hfan@iphy.ac.cn

I. MODEL AND HAMILTONIAN

We focus on the generalized one-dimensional (1D) Aubry-André-Harper (AAH) model [1–4]. The total Hamiltonian of the system is

$$\hat{H}_{\text{AAH}} = \sum_{j=1}^{N} v \cos(2\pi b_v j + \varphi_v)\hat{a}_j^\dagger \hat{a}_j + \sum_{j=1}^{N-1} u\left[1 + \lambda \cos(2\pi b_\lambda j + \varphi_\lambda)\right](\hat{a}_j^\dagger \hat{a}_{j+1} + \hat{a}_j \hat{a}_{j+1}^\dagger), \tag{S1}$$

where $\hat{a}$ ($\hat{a}^\dagger$) denotes the annihilation (creation) operator, and v (λ) is the strength of the cosine modulations on the frequencies (hopping couplings) with a periodicity $1/b_v$ ($1/b_\lambda$) and phase factor φ_v (φ_λ). The special case with $\lambda = 0$ ($v = 0$) corresponds to the diagonal (off-diagonal) AAH model. For convenience, we set $\hbar = 1$ throughout the paper.

Here, we use a 1D array of 43 programmable superconducting qubits to simulate the generalized AAH model. The fabrication and experimental setup are introduced in Sec. II. Our system can be well described by the Hamiltonian of the Bose-Hubbard model:

$$\hat{H}_{\text{BH}} = \sum_{j=1}^{N} \omega_j \hat{a}_j^\dagger \hat{a}_j + \sum_{j=1}^{N} \frac{\alpha_j}{2} \hat{a}_j^\dagger \hat{a}_j^\dagger \hat{a}_j \hat{a}_j + \sum_{j=1}^{N-1} g_{j,j+1}(\hat{a}_j^\dagger \hat{a}_{j+1} + \hat{a}_j \hat{a}_{j+1}^\dagger), \tag{S2}$$

where $\hat{a}_j$ ($\hat{a}_j^\dagger$) denotes the bosonic annihilation (creation) operator of the j-th qubit, $g_{j,j+1}$ is the nearest-neighbor (NN) coupling strength, ω_j denotes the qubit frequency, and α_j represents anharmonicity. With $|\alpha_j| \gg |g_{j,j+1}|$, the Hamiltonian is reduced to the XX model

$$\hat{H} = \sum_{j=1}^{N} \omega_j \hat{\sigma}_j^+ \hat{\sigma}_j^- + \sum_{j=1}^{N-1} g_{j,j+1}(\hat{\sigma}_j^+ \hat{\sigma}_{j+1}^- + \hat{\sigma}_j^- \hat{\sigma}_{j+1}^+), \tag{S3}$$

where $\hat{\sigma}_j^+$ ($\hat{\sigma}_j^-$) is the raising (lowering) operator. In this low-filling case, to realize the AAH model:

$$\omega_j = \omega_{\text{ref}} + v \cos(2\pi b_v j + \varphi_v), \tag{S4}$$

$$g_{j,j+1}^{\text{eff}} = u\left[1 + \lambda \cos(2\pi b_\lambda j + \varphi_\lambda)\right], \tag{S5}$$

where ω_{ref} denotes the reference frequency. In this work, we use Floquet engineering to adjust the effective coupling $g_{j,j+1}^{\text{eff}}$. The experimental details of Floquet engineering are shown in Sec. III and the automatic calibration for the frequencies and couplings are presented in Sec. V.

II. FABRICATION AND EXPERIMENTAL SETUP

The 43-qubit *Chuang-tzu* sample used in this work is fabricated on a 430 μm thick sapphire chip with standard wafer cleaning. Specifically, a layer of 100 nm Al was firstly deposited on a 15×15 mm^2 sapphire substrate and patterned with optical lithography using 0.70 μm of positive SPR955 resist. Then, we used wet etching to produce large structures, such as microwave coplanar waveguide resonators, transmission lines, control lines, and capacitors of the transmon qubits. The Josephson junctions definition process consists of patterning a bilayer of MMA and PMMA resists with electron beam lithography, which were made using double-angle evaporation with a 65 nm thick Al layer at $+60°$, followed by several minutes oxidation in pure oxygen, and a 100 nm thick second layer of Al at $0°$. Finally, in order to suppress the parasitic modes, a number of airbridges [5] are constructed on the chip. The optical micrograph of the whole chip is displayed in Fig. S1.

We optimize the end (near the qubit) of the XY/Z control lines by extending the end away from the qubits and then ground to reduce the crosstalk to other qubits due to the microwave signal and flux bias. Normally, the control line is grounded directly at the end, but the microwave signal does not disappear instantly and continues to propagate along the metal. If the spatial distance between the qubits is not far enough, it is easy to cause the microwave signal propagating to the neighboring qubits and generate the crosstalk. By extending the end of the control lines to ensure that their grounded ports are away from the qubits, the leaked microwave signal can be kept away from the qubits, reducing the microwave crosstalk. At the same time, for DC bias, the extended control lines can generate a current in the opposite direction to the incoming current, generating mutually offset magnetic flux and effectively reducing the flux crosstalk. The Z crosstalk matrix is shown in Fig. S2.

To implement experimental measurements, our superconducting quantum chip is placed in a BlueFors dilution refrigerator with a mixing chamber (MC) at a temperature of about 20 mK. The typical wiring of the control electronics and cryogenic equipment is shown in Fig. S3. There are 5 readout transmission lines, each of which is equipped with a superconducting
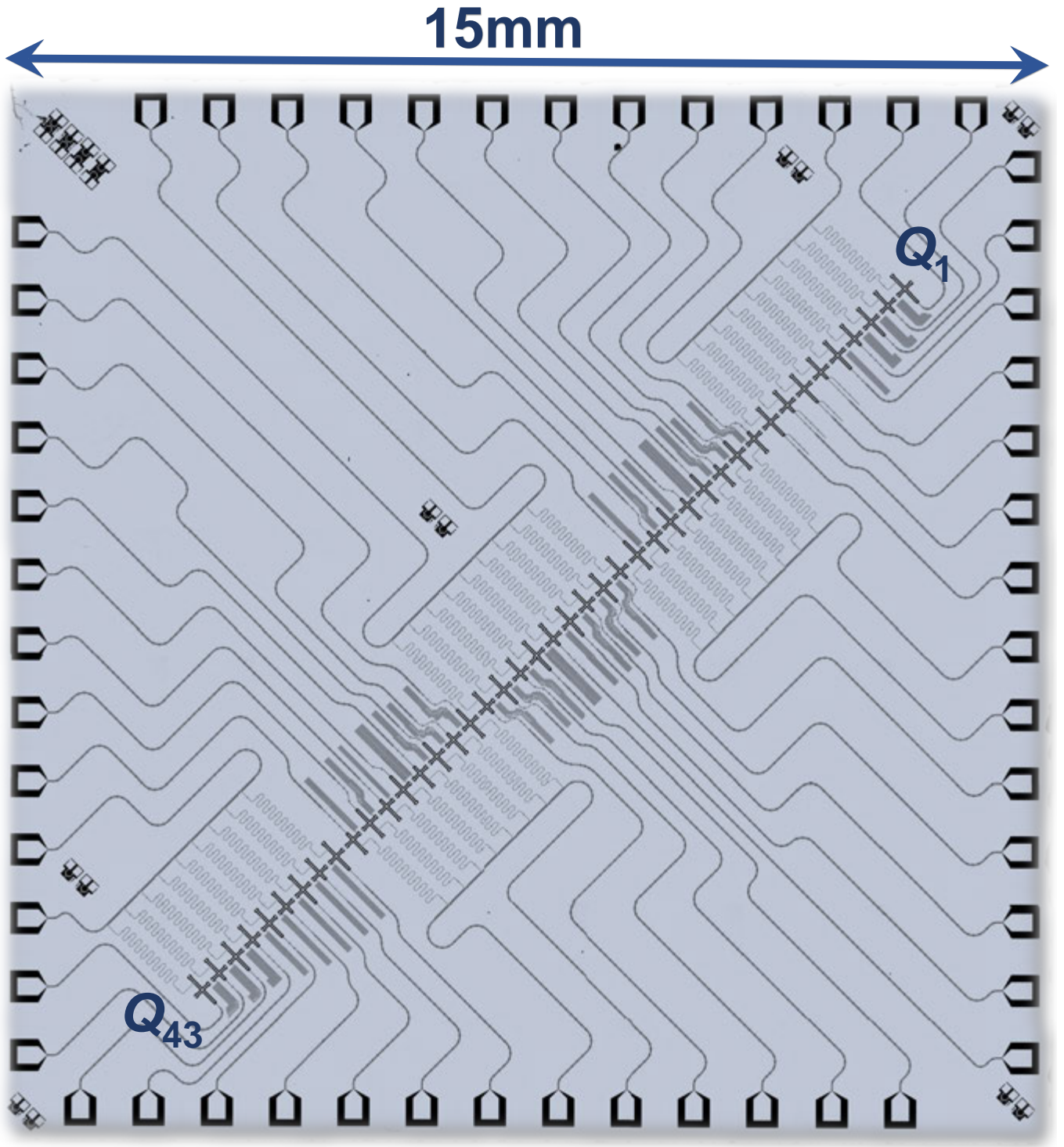
FIG. S1. The optical micrograph of the 43-qubit sample. Each qubit has only one control line for the combined XY and Z controls.

Josephson parametric amplifier (JPA), a cryo low-noise amplifier (LNA), and a room-temperature RF amplifier (RFA). The readout pulse on the transmission line is first generated by a microwave arbitrary waveform generator (AWG) consisting of two digital-analog converter (DAC) channels and a local oscillation (LO), then amplified by the amplifiers at different temperatures after interacting with the chip, and finally modulated by the analog-digital converter (ADC).

In order to reduce the number of cryogenic control lines in the refrigerator, we combine the high-frequency microwave
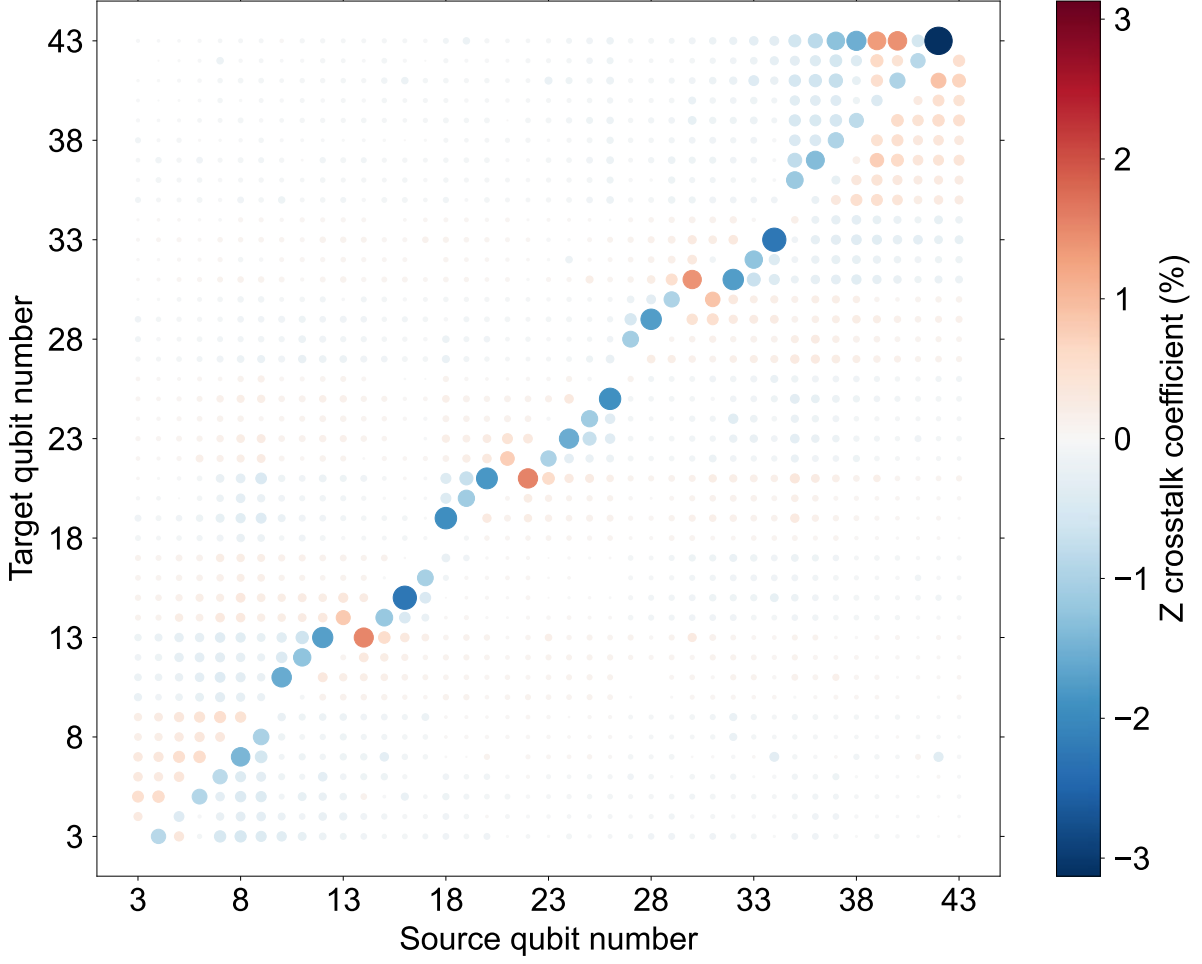
FIG. S2. Z crosstalk matrix. The size of each bubble indicates the absolute value of the Z crosstalk matrix element of its corresponding source qubit to the target qubit. Except the crosstalk of Q_{42} to Q_{43}, which is 3.13%, all the remaining crosstalk coefficients are less than 2.26%

excitation signal with the low-frequency bias signal by using directional couplers at room temperature, so that the XY and Z control lines of the qubits are merged into one at cryogenic temperature. Moreover, we set a microwave switch at each LO port, which is controlled by the experimental trigger signal, to suppress the thermal excitation originating from the continuous microwave signal. We also perform zero calibration of every AWG to reduce intrinsic and mirror leakages.

Our superconducting quantum processor consists of 43 transmon qubits ($Q_1, \cdots, Q_{43}$) arrayed in a row, where each qubit is capacitively coupled to its nearest neighbors with a mean hopping strength of about 7.6 MHz. The typical device parameters are briefly shown in Table S1. Here, we used $Q_3, \cdots, Q_{43}$ (relabeled as $Q_1, \cdots, Q_{41}$) for the 41-qubit experiment, and Q_4, $\cdots, Q_{43}$ (relabeled as $Q_1, \cdots, Q_{40}$) for the 40-qubit experiment, but note that their idle points are the same, and the operating points during the experiments are different. The mean energy relaxation time $\overline{T}_1$ of the 41 qubits is 21.0 μs. To utilize Floquet engineering to tune the effective hopping strengths, we calibrate the qubits to idle frequencies at an average of about 660 MHz away from their respective maximum frequencies, so that the amplitudes of the time-periodic driving can be adjusted over a wide range. To suppress the dephasing of low-frequency qubits, all the Z control lines are equipped with DC blocks, and the mean pure dephasing time at the idle frequency is 1.2 μs.
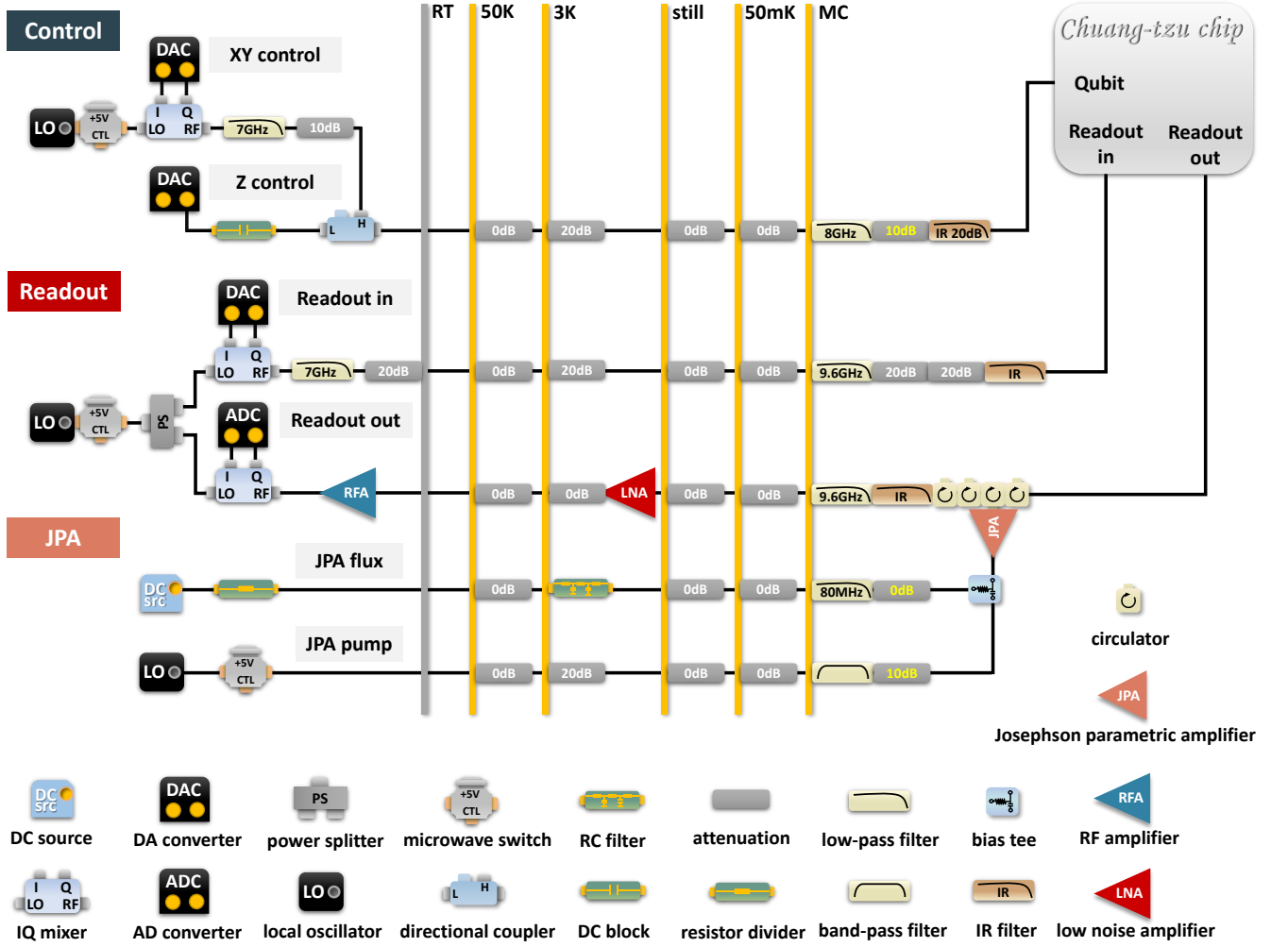
FIG. S3. A schematic diagram of the experimental system and wiring information. Here, MC refers to mixing chamber, RFA is the room-temperature RF amplifier, LNA denotes the low-noise amplifier, and JPA is the Josephson parametric amplifier.

III. FLOQUET ENGINEERING OF SUPERCONDUCTING CIRCUITS

A. Time-periodic driving and effective hopping strength

Floquet engineering has been shown as an effective method to adjust hopping strengths in superconducting quantum circuits [6, 7]. It requires the time-periodic drivings on qubits frequencies as

$$\omega(t) = \overline{\omega} + A\sin(\mu t + \varphi), \tag{S6}$$

where A, μ, and φ denote the modulation amplitude, frequency, and phase, respectively. Here, $\overline{\omega}$ is the average frequency of qubit, which holds a constant ω_{ref} for all the resonant qubits in our experiments concerning the off-diagonal AAH model. For convenience, we set $\mu/2\pi = 80$ MHz for all the qubits.

Without loss of generality, we first show a two-qubit example. The two-qubit Hamiltonian with nearest-neighbor hopping interaction can be written as

$$\hat{H}(t) = \omega_1(t)\hat{n}_1 + \omega_2(t)\hat{n}_2 + g(\hat{a}_1^\dagger \hat{a}_2 + \hat{a}_1 \hat{a}_2^\dagger), \tag{S7}$$

where $\hat{n}_j \equiv \hat{a}_j^\dagger \hat{a}_j$ is the number operator, $\hat{a}_j$ ($\hat{a}_j^\dagger$) denotes the annihilation (creation) operator of the j-th qubit, $\omega_j(t)$ denotes the modulated qubit frequency, and g is the direct coupling strength. Here, we use the interaction picture. The corresponding

Parameter	Median	Mean	Stdev.	Units
Qubit maximum frequency	5.767	5.914	0.280	GHz
Qubit idle frequency	5.091	5.254	0.413	GHz
Qubit anharmonicity $\alpha/2\pi$	-0.202	-0.216	0.021	GHz
Readout frequency	6.684	6.680	0.05	GHz
Mean energy relaxation time $\overline{T}_1$	20.9	21.0	6.0	μs
Pure dephasing time at idle frequency T_2^*	1.1	1.2	0.4	μs
Qubit-resonator coupling	35.3	34.9	3.8	MHz
Mean fidelity of single-qubit gates	99.2	99.0	1.3	%

TABLE S1. List of device parameters.

unitary transformation is

$$\hat{U}_{\mathrm{I}}(t) = \exp\left\{ \mathrm{i}\left[\overline{\omega}t - \frac{A_1}{\mu}\cos\left(\mu t + \varphi_1\right)\right]\hat{n}_1 + \mathrm{i}\left[\overline{\omega}t - \frac{A_2}{\mu}\cos\left(\mu t + \varphi_2\right)\right]\hat{n}_2 \right\},\tag{S8}$$

where the qubits frequencies take the forms of Eq. S6. Hence, the effective Hamiltonian can be calculated as

$$\begin{aligned}
\hat{H}_{\mathrm{I}} &= \hat{U}_{\mathrm{I}}(t)\hat{H}(t)\hat{U}_{\mathrm{I}}^\dagger(t) + \mathrm{i}\left(\frac{\mathrm{d}}{\mathrm{d}t}\hat{U}_{\mathrm{I}}(t)\right)\hat{U}_{\mathrm{I}}^\dagger(t),\\
&= g\exp\left[\mathrm{i}\frac{A_1}{\mu}\cos(\mu t + \varphi_1)\right]\exp\left[-\mathrm{i}\frac{A_2}{\mu}\cos(\mu t + \varphi_2)\right]\hat{a}_1^\dagger\hat{a}_2 + \mathrm{H.c.},\\
&= g\sum_{m,n=-\infty}^{+\infty}\mathrm{i}^{m+n}J_m\left(\frac{A_1}{\mu}\right)J_n\left(-\frac{A_2}{\mu}\right)\exp\left[\mathrm{i}(m+n)\mu t\right]\exp\left[\mathrm{i}(m\varphi_1 + n\varphi_2)\right]\hat{a}_1^\dagger\hat{a}_2 + \mathrm{H.c.},\\
&\approx g\sum_{m=-\infty}^{+\infty}J_m\left(\frac{A_1}{\mu}\right)J_{-m}\left(-\frac{A_2}{\mu}\right)\exp\left[\mathrm{i}m(\varphi_1 - \varphi_2)\right]\hat{a}_1^\dagger\hat{a}_2 + \mathrm{H.c.},
\end{aligned}\tag{S9}$$

where the second line is obtained by using the Baker-Hausdorff formula $e^{\mathrm{i}x\hat{a}^\dagger\hat{a}}f(\hat{a}^\dagger,\hat{a})e^{-\mathrm{i}x\hat{a}^\dagger\hat{a}} = f(\hat{a}^\dagger e^{\mathrm{i}x}, \hat{a}e^{-\mathrm{i}x})$, the third line uses the Jacobi-Anger series $e^{\mathrm{i}x\cos\theta} = \sum_{m=-\infty}^{+\infty}\mathrm{i}^m J_m(x)e^{\mathrm{i}m\theta}$, with J_m being the m-order Bessel function of the first kind, and the last line follows from the rotating-wave approximation with the bound constraint $m+n=0$. Thus, the effective hopping strength can be expressed as

$$g^{\mathrm{eff}} = g\sum_{m=-\infty}^{+\infty}J_m\left(\frac{A_1}{\mu}\right)J_{-m}\left(-\frac{A_2}{\mu}\right)\exp\left[\mathrm{i}m(\varphi_1 - \varphi_2)\right].\tag{S10}$$

In the following, we discuss three special cases.

(i) $\varphi_1 - \varphi_2 = 2n\pi$, with n being an integer. By using $J_m(x+y) = \sum_{l=-\infty}^{+\infty}J_l(x)J_{m-l}(y)$, Eq. S10 is reduced as

$$g^{\mathrm{eff}} = gJ_0\left(\frac{A_1 - A_2}{\mu}\right).\tag{S11}$$

(ii) $\varphi_1 - \varphi_2 = (2n+1)\pi$, with n being an integer. Similarly, we can obtain

$$g^{\mathrm{eff}} = gJ_0\left(\frac{A_1 + A_2}{\mu}\right),\tag{S12}$$

based on the parity of the Bessel function $J_m(x) = J_m(-x)$ and $J_m(x) = (-1)^m J_{-m}(x)$.

(iii) $A_1 = A \neq 0$, $A_2 = 0$. In this case, there is only one time-periodic driving and the effective hopping strength is given by

$$g^{\mathrm{eff}} = gJ_0\left(\frac{A}{\mu}\right).\tag{S13}$$

Based on the properties of the Bessel function, the decoupling point is reached when $A \approx 2.405\mu$, and the maximum coupling is $g^{\mathrm{eff}} \approx -0.403g$ with $A \approx 3.832\mu$. In our devices, g is around 7.6 MHz, so the adjustable range of coupling strength is from -3.06 MHz to 7.6 MHz.

Although the above results are derived for the two-qubit case, the formulas are applicable for the multi-qubit case, and the couplings of the driven qubit to readout resonator and XY microwave can be described by this simplified model.
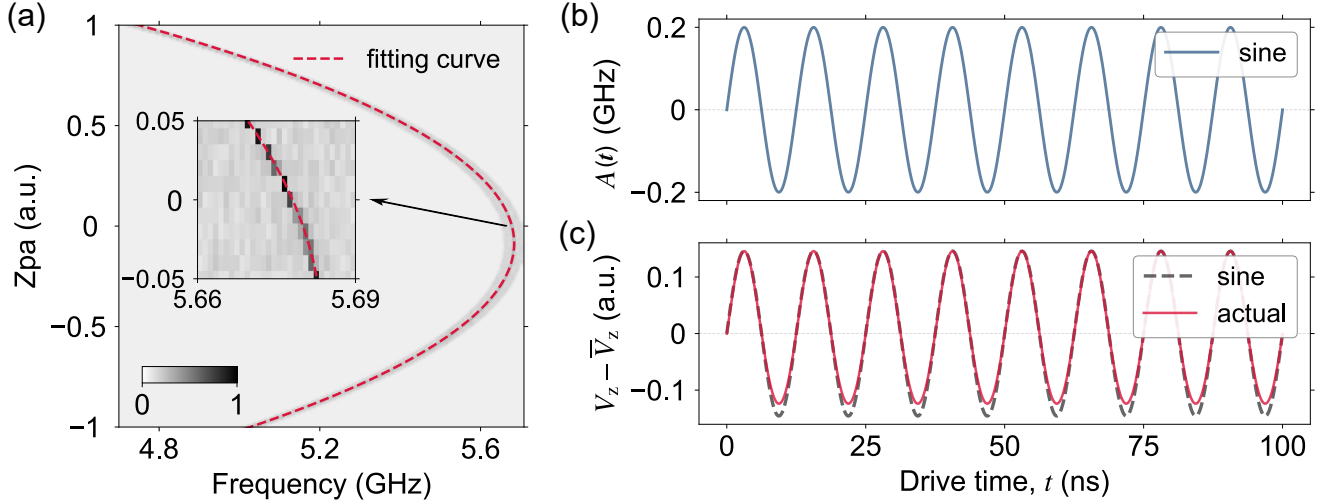
FIG. S4. Single-qubit spectroscopy and Floquet Z pulse. (a) Typical experimental data of single-qubit spectroscopy. The red dashed line is for the fitting result in the form of Eq. S14. (b) Sine modulation in the frequency with $A/(2\pi) = 0.2$ GHz and $\mu/(2\pi) = 80$ MHz. (c) The corresponding modulated Zpa. Here the red solid line is the actual Zpa used in the Floquet engineering, while the gray dashed line represents a sine-like Zpa.

B. Amplitude modulation

According to Eqs. (S6, S11–S13), the effective hopping strength depends on the driving amplitude with respect to the qubit frequency. In order to accurately manipulate the hopping strength, we need to calibrate the mapping between the qubit frequency and the experimental Z pulse amplitude (Zpa).

For the frequency-tunable transmon qubit with symmetric Josephson junctions, the relationship between qubit frequency ω and external flux Φ_e is given by [8]

$$\omega = \sqrt{8E_{\mathrm{JJ}}E_{\mathrm{C}}\left|\cos(\pi\frac{\Phi_e}{\Phi_0})\right|} - E_{\mathrm{C}}, \tag{S14}$$

where E_{vJJ} denotes the Josephson energy when no flux enters the loop of the superconducting quantum interference device (SQUID), E_{C} is the charging energy, and Φ_0 denotes the flux quantum. The external flux Φ_e is linearly related to the Zpa V_z on the qubit produced by the DC source or AWG under the weak flux conditions, i.e., $\pi\Phi_e/\Phi_0 = kV_z + b$. Here, E_{C} can be determined by performing a double-photon excitation experiment, and other parameters E_{JJ}, k, and b can be obtained by fitting the spectroscopy measurement results of the qubit, see Fig. S4(a). Hence, we can obtain the relationship between the Zpa V_z and the driving amplitude A by substituting Eq. S14 into Eq. S6:

$$V_z = \frac{1}{k}\arccos\left[\pm\frac{(\overline{\omega} + A\sin(\mu t + \varphi) + E_C)^2}{8E_{\mathrm{JJ}}E_{\mathrm{C}}}\right] - \frac{b}{k},$$

$$= \frac{1}{k}\arccos\left[\pm\frac{\left(\sqrt{8E_{\mathrm{JJ}}E_{\mathrm{C}}\left|\cos(k\overline{V}_z + b)\right|} + A\sin(\mu t + \varphi)\right)^2}{8E_{\mathrm{JJ}}E_{\mathrm{C}}}\right] - \frac{b}{k}, \tag{S15}$$

where $\overline{V}_z$ is the constant amplitude of a rectangular Zpa without any modulations ($A = 0$ GHz), which makes the qubit frequency equal to $\overline{\omega}$. Thus, given the driving amplitude, we can then calculate the corresponding Zpa and construct the actual Z pulse waveform, see Fig. S4, (b) and (c).

To evaluate the actual coupling strength between two qubits, we perform a swap-like experiment. First, we identify the Zpa of each qubit to make them resonant and then add the time-periodic driving on one of the qubits. As the driving amplitude A increases, the period of the swap changes, but at the same time, the swap probability becomes smaller, as shown in Fig. S5(a). This is due to the frequency of the driven qubit gradually deviating from the resonance point. We correct this frequency detuning
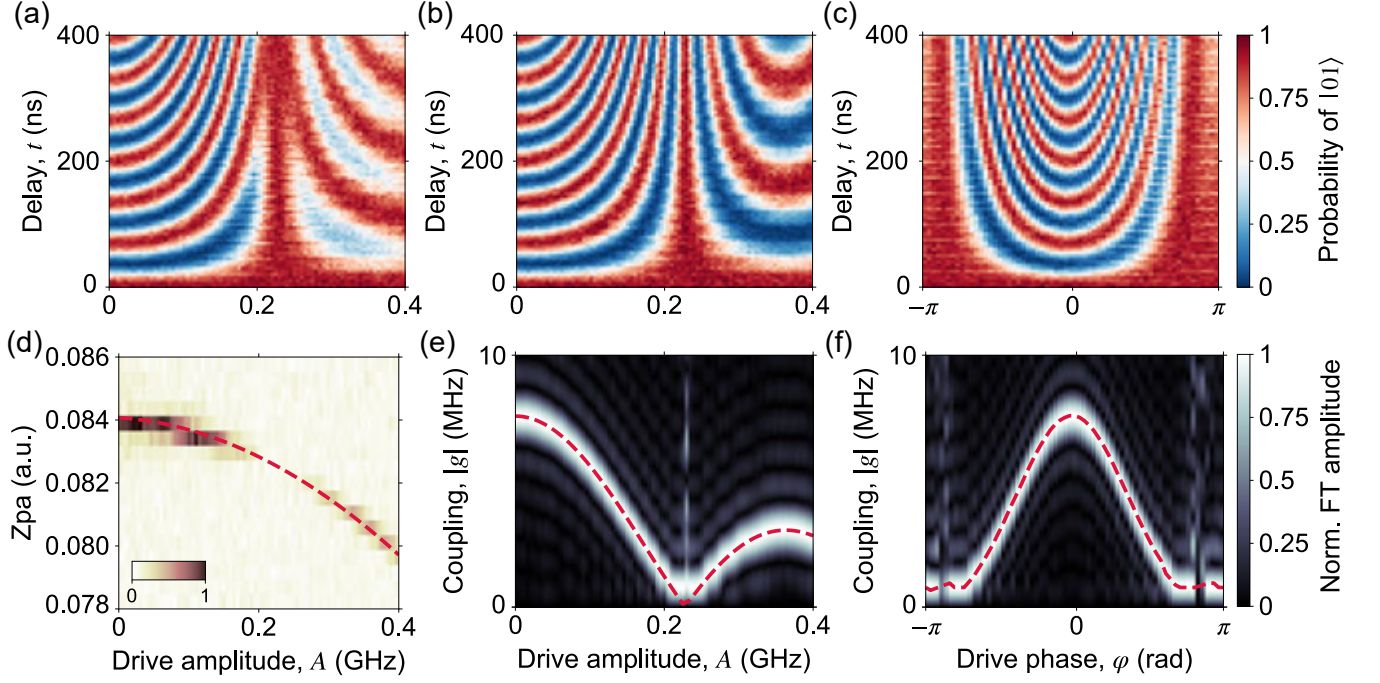
FIG. S5. Amplitude modulation and phase alignment of Floquet engineering. Here we fix $\mu/(2\pi) = 80$ MHz. (a) Swap probability of $|10\rangle$ with the time-periodic driving before correcting the qubit frequency detuning. (b) Swap probability of $|10\rangle$ after correcting the qubit frequency detuning. (c) Phase alignment between two qubits. Both driving amplitudes are set to 0.1 GHz. (d) Spectroscopic measurement of the qubit frequency detuning induced by the modulation of the Z pulse. The red dashed curve is the polynomial fitting result of the relationship between the driving amplitude and the compensation Zpa. (e) Coupling strength versus the driving amplitude, which is extracted from the FT of (b). The red dashed curve denotes the fitting result in the form of the Bessel function. (f) Coupling strength versus drive phase, which is extracted from the FT of (c). The phase corresponding to the maximum coupling strength is the phase difference to be compensated. Here we determine this phase by a polynomial fitting shown by the red dashed curve.

by fitting the results of scanning the compensation Zpa and the driving amplitude with a polynomial, as shown in Fig. S5(d). Note that the probability of readout becomes smaller as the driving amplitude approaches the decoupling point. Because the couplings of the driven qubit to readout resonator and XY microwave are also modulated, except that the resonance conditions are not satisfied here and the rotation wave approximation may be excluded.

After this correction, we obtain a better swap probability result, as shown in Fig. S5(b). In the experiments, we use Eq. S15 to estimate the relationship between the driving amplitude and the Zpa, and apply the Bessel function in Eq. S13 to calculate the hopping strength. However, considering the control deviation, we need to add a scale factor η (≈ 1) into the Bessel function, and the effective hopping strength is expressed as

$$g^{\text{eff}} = gJ_0\left(\eta\frac{A}{\mu}\right). \tag{S16}$$

The above formula is used to fit the mapping between the driving amplitude and the coupling strength, as displayed in Fig. S5(e). The experimental couplings are calculated as half the Fourier frequency of the swap probability of $|01\rangle$ (or $|10\rangle$).

C. Phase alignment

In our experiments, we modulate the coupling strengths between each pair of neighboring qubits to realize the off-diagonal AAH model. All qubits are simultaneously driven by the time-periodic Z pulse. The modulated coupling strength satisfies

$$g^{\text{eff}}_{j,j+1} = g_{j,j+1} \sum_{m=-\infty}^{+\infty} J_m\left(\frac{\eta_j A_j}{\mu}\right) J_{-m}\left(-\frac{\eta_{j+1} A_{j+1}}{\mu}\right) \exp\left[im(\varphi_j - \varphi_{j+1})\right] \tag{S17}$$

where the phase difference is $\Delta\varphi_j = \varphi_j - \varphi_{j+1}$. Compared with Eq. S10, Eq. S17 is modified by two scale factors η_j and η_{j+1}, which are determined by fitting the amplitude modulation curves. Similar to Eq. S11, the effective coupling is given by
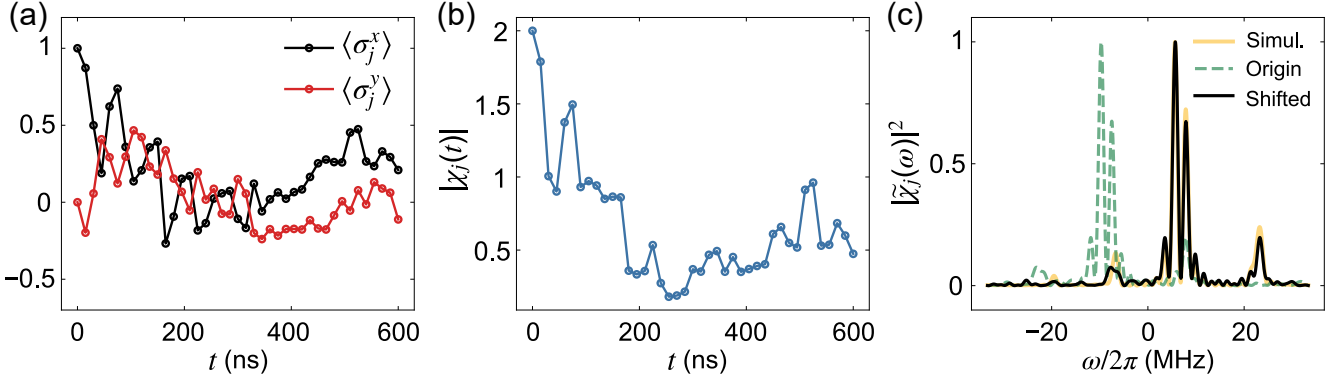
FIG. S6. Typical experimental data of the single-qubit Loschmidt echo. (a) Pauli expectations $\langle\hat{\sigma}^x(t)\rangle$ and $\langle\hat{\sigma}^y(t)\rangle$ versus the evolution time t. (b) The magnitude of the Loschmidt echo amplitude versus the evolution time t. (c) Fourier spectrum of the Loschmidt echo amplitude.

the following formula with $\Delta\varphi_j = 0$

$$g_{j,j+1}^{\text{eff}} = g_{j,j+1} J_0\left(\frac{\eta_j A_j - \eta_{j+1} A_{j+1}}{\mu}\right). \tag{S18}$$

Note that when the driving amplitudes of the two qubits meet $\eta_j A_j = \eta_{j+1} A_{j+1}$, the coupling strength reaches its maximum value $g_{j,0}$. We perform the phase alignment calibration in this condition and scan the drive phase of one qubit to measure the period of the two-qubit swap. If the phase is aligned, the coupling strength will be the maximum $g_{j,0}$. We figure out this point and compensate this drive phase into the time-periodic driving of the corresponding qubit. The typical experimental data is shown in Fig. S5, (c) and (f). It can be seen that for the devices that have been calibrated for the timing of the Z pulses, the compensation of the drive phase is almost zero.

IV. ENERGY SPECTRUM MEASUREMENT

A. Loschmidt echo and Fourier spectrum

The Loschmidt echo (LE) of qubit j is defined as $\mathcal{L}_j(t) = |\chi_j(t)|^2$, where the amplitude is given by

$$\chi_j(t) = \langle 2\hat{\sigma}_j^+(t)\rangle = \langle\hat{\sigma}_j^x(t)\rangle + \mathrm{i}\langle\hat{\sigma}_j^y(t)\rangle. \tag{S19}$$

Here the average is taken with respect to the time-evolved state

$$|\Psi(t)\rangle_j = e^{-\mathrm{i}\hat{H}t}|\Psi(0)\rangle_j = \sum_n C_{n,j} e^{-\mathrm{i}E_n t}|\phi_n\rangle, \tag{S20}$$

by virtue of the time-dependent Schrödinger equation, where $C_{n,j} = \langle\phi_n|\Psi(0)\rangle_j$ and the spectral decomposition of the total Hamiltonian is $H = \sum_n E_n|\phi_n\rangle\langle\phi_n|$.

Considering the single-excitation case, we choose the initial state that is prepared by a $Y_{\pi/2}$ gate on qubit j:

$$|\Psi(0)\rangle_j = |0\rangle_1 \otimes |0\rangle_2 \otimes \cdots \frac{1}{\sqrt{2}}\left(|0\rangle_j + |1\rangle_j\right) \otimes \cdots |0\rangle_{N-1} \otimes |0\rangle_N, \tag{S21}$$

and measure the expectation $\langle\hat{\sigma}_j^x(t)\rangle$ and $\langle\hat{\sigma}_j^y(t)\rangle$ to obtain the amplitude of LE by Eq. S19 (see typical experimental data in Fig. S6, (a) and (b)). In the absence of any decoherence or noise, $\chi_j(t)$ can be calculated as

$$\chi_j(t) = \sum_n |C_{n,j}|^2 e^{-\mathrm{i}E_n t}, \tag{S22}$$

and the information about the energy spectrum is encoded in its Fourier transform (FT)

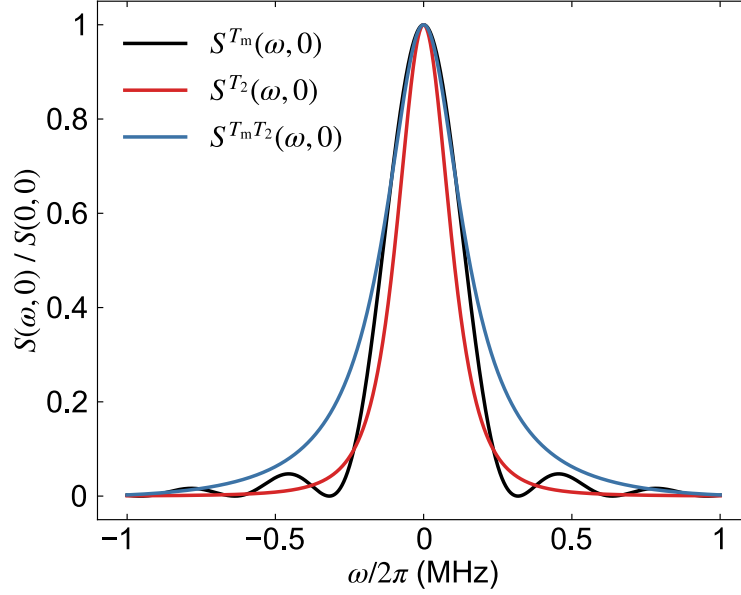$$\widetilde{\chi}_j(\omega) = \mathscr{F}\{\chi_j(t)\} = \sum_n |C_{n,j}|^2 \delta(\omega - E_n), \tag{S23}$$

FIG. S7. Effects of both the measurement time window and decoherence on the Fourier spectrum. Here we set $T_{\mathrm{m}} = T_2 = 1$ μs.

where $\mathscr{F}\{\cdot\}$ denotes the Fourier transform and $\delta(\cdot)$ is the Dirac delta function. Although the corresponding peak of each eigenenergy E_n is included in Eq. S23, we are still unable to directly obtain all the spectral information just from one single-qubit result because the coefficient $C_{n,j}$ could be too small, and for some particular eigenenergy E_n this coefficient may be too large that it overwhelms other peaks. Therefore, we select a few qubits and sum the squared magnitudes of their $\widetilde{\chi}_j(\omega)$ as

$$I(\omega) = \sum_j |\widetilde{\chi}_j(\omega)|^2 , \tag{S24}$$

thus the positions of the peaks in $I(\omega)$ indicate the energy spectrum of the total Hamiltonian. In fact, these peaks are widened due to the measurement time window and decoherence, as explained in the following.

B. Measurement time window and decoherence

(*i*) Only considering the effects of the measurement time window. Considering the finite length of the measurement time window $[0, T_{\mathrm{m}}]$ for acquiring experimental data, we rewrite the LE amplitude as

$$\chi_j^{T_{\mathrm{m}}}(t) = \sum_n |C_{n,j}|^2 e^{-\mathrm{i}E_n t}\mathrm{rect}\left(\frac{t - \frac{T_{\mathrm{m}}}{2}}{T_{\mathrm{m}}}\right) , \tag{S25}$$

where $\mathrm{rect}(\cdot)$ is the rectangular time window function. Hence, its FT can be expressed as

$$\begin{aligned}
\widetilde{\chi}_j^{T_{\mathrm{m}}}(\omega) &= \mathscr{F}\left\{\sum_n |C_{n,j}|^2 e^{-\mathrm{i}E_n t}\right\} * \mathscr{F}\left\{\mathrm{rect}\left(\frac{t - \frac{T_{\mathrm{m}}}{2}}{T_{\mathrm{m}}}\right)\right\} \\
&= \sum_n |C_{n,j}|^2 \delta(\omega - E_n) * \exp\left(-\mathrm{i}\omega\frac{T_{\mathrm{m}}}{2}\right) T_{\mathrm{m}}\mathrm{sinc}\left(\omega\frac{T_{\mathrm{m}}}{2}\right) \\
&= \sum_n |C_{n,j}|^2 \exp\left[-\mathrm{i}(\omega - E_n)\frac{T_{\mathrm{m}}}{2}\right] T_{\mathrm{m}}\mathrm{sinc}\left[(\omega - E_n)\frac{T_{\mathrm{m}}}{2}\right] ,
\end{aligned} \tag{S26}$$

where $*$ denotes the convolution, the first line follows from the convolution theorem of the FT and the third line follows from $\delta(x - x_0) * f(x) = f(x - x_0)$. To evaluate the peak broadening of $I(\omega)$ around $\omega = E_n$ due to the measurement time window,
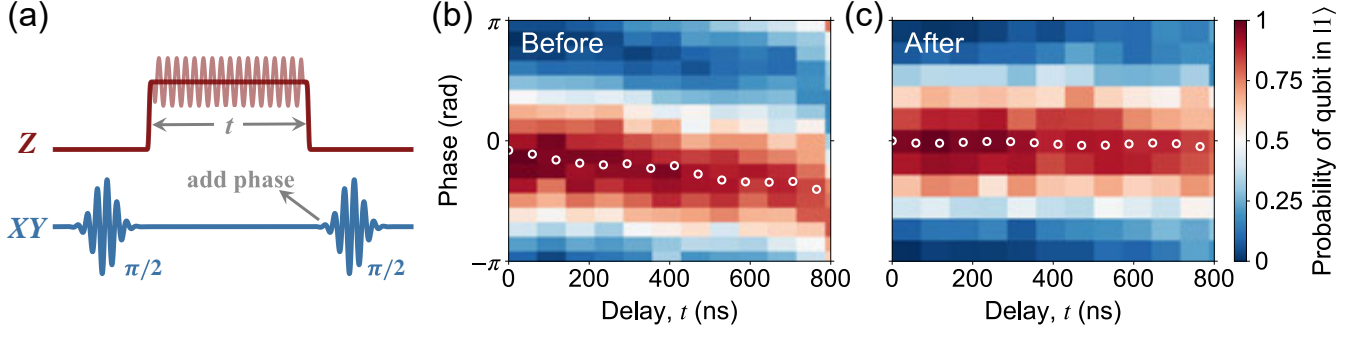
FIG. S8. Phase calibration. (a) The Ramsey-like pulse sequence of measuring the phase accumulation. The experimental results show the $|1\rangle$-state probability evolution before (b) and after (c) the phase compensation, respectively.

we define the profile function

$$S^{T_{\mathrm{m}}}(\omega, E_n) = \left| \exp\left[-i(\omega - E_n)\frac{T_{\mathrm{m}}}{2} \right] T_{\mathrm{m}} \mathrm{sinc}\left[(\omega - E_n)\frac{T_{\mathrm{m}}}{2} \right] \right|^2 = T_{\mathrm{m}}^2 \mathrm{sinc}^2\left[(\omega - E_n)\frac{T_{\mathrm{m}}}{2} \right], \tag{S27}$$

and calculate its full width at half maximum (FWHM):

$$\Delta\omega_{T_{\mathrm{m}}} \approx \frac{5.57}{T_{\mathrm{m}}}, \quad \Delta f_{T_{\mathrm{m}}} = \frac{\Delta\omega_{T_{\mathrm{m}}}}{2\pi} \approx \frac{0.89}{T_{\mathrm{m}}}. \tag{S28}$$

(ii) Only considering the effects of decoherence. As the evolution time increases, one can observe an exponential decay of the LE amplitude due to the decoherence process in the experiments with a decaying rate γ

$$\chi_j^{T_2}(t) = \sum_n |C_{n,j}|^2 e^{-iE_n t} \exp(-\gamma|t|). \tag{S29}$$

Here $\gamma = 1/T_2 = 1/(2T_1) + 1/T_2^*$, with T_1 and T_2^* being the energy relaxation time and the pure dephasing time of the measured qubit j, respectively. The FT of $\chi_j^{T_2}(t)$ is given by

$$\begin{aligned}
\widetilde{\chi}_j^{T_2}(\omega) &= \mathscr{F}\left\{ \sum_n |C_{n,j}|^2 e^{-iE_n t} \right\} * \mathscr{F}\left\{ \exp(-\gamma|t|) \right\} \\
&= \sum_n |C_{n,j}|^2 \delta(\omega - E_n) * \frac{2\gamma}{\gamma^2 + \omega^2} \\
&= \sum_n |C_{n,j}|^2 \frac{2\gamma}{\gamma^2 + (\omega - E_n)^2} \\
&= \sum_n |C_{n,j}|^2 \frac{\frac{2}{T_2}}{(\frac{1}{T_2})^2 + (\omega - E_n)^2},
\end{aligned} \tag{S30}$$

and the corresponding profile function becomes

$$S^{T_2}(\omega, E_n) = \frac{(\frac{2}{T_2})^2}{\left[(\frac{1}{T_2})^2 + (\omega - E_n)^2 \right]^2}, \tag{S31}$$

with the FWHM

$$\Delta\omega_{T_2} = \frac{2\sqrt{\sqrt{2} - 1}}{T_2} \approx \frac{1.29}{T_2}, \quad \Delta f_{T_2} = \frac{\Delta\omega_{T_2}}{2\pi} = \frac{\sqrt{\sqrt{2} - 1}}{\pi T_2} \approx \frac{0.2}{T_2}. \tag{S32}$$

(*iii*) Considering both the effects of measurement time window and decoherence. Taking into account both the effects of measurement time window and decoherence, we rewrite the FT of LE amplitude as

$$
\widetilde{\chi}_j^{T_{\mathrm{m}}T_2}(\omega) = \mathscr{F}\left\{\sum_n |C_{n,j}|^2 e^{-\mathrm{i}E_n t}\right\} * \mathscr{F}\left\{\mathrm{rect}\left(\frac{t-\frac{T_{\mathrm{m}}}{2}}{T_{\mathrm{m}}}\right)\exp(-\gamma|t|)\right\}
$$

$$
= \sum_n |C_{n,j}|^2 \frac{\frac{2}{T_2}}{(\frac{1}{T_2})^2+(\omega-E_n)^2}\exp\left(-\mathrm{i}\omega\frac{T_{\mathrm{m}}}{2}\right)
$$

$$
\times\left[1+e^{-\frac{T_{\mathrm{m}}}{2T_2}}\left((\omega-E_n)T_2\sin\left[(\omega-E_n)\frac{T_{\mathrm{m}}}{2}\right]-\cos\left[(\omega-E_n)\frac{T_{\mathrm{m}}}{2}\right]\right)\right] \tag{S33}
$$

with the corresponding profile function

$$
S^{T_{\mathrm{m}}T_2}(\omega,E_n)=\frac{\left(\frac{2}{T_2}\right)^2\left[1+e^{-\frac{T_{\mathrm{m}}}{2T_2}}\left((\omega-E_n)T_2\sin\left[(\omega-E_n)\frac{T_{\mathrm{m}}}{2}\right]-\cos\left[(\omega-E_n)\frac{T_{\mathrm{m}}}{2}\right]\right)\right]^2}{\left[(\frac{1}{T_2})^2+(\omega-E_n)^2\right]^2}. \tag{S34}
$$

It can be verified that

$$
\lim_{T_2\to\infty}S^{T_{\mathrm{m}}T_2}=S^{T_{\mathrm{m}}}, \qquad \lim_{T_{\mathrm{m}}\to\infty}S^{T_{\mathrm{m}}T_2}=S^{T_2}. \tag{S35}
$$

In Fig. S7, we show the effects of the measurement time window and decoherence on the Fourier spectrum.

According to the above discussion, the FWHM (the precision in the energy spectrum measurement) is limited by the measurement time length and the decoherence time. In our experiments, the decoherence time only limits how long we can track the LE amplitude oscillations, which will ultimately bound the maximum precision in the Fourier spectrum. If the decoherence time is determined, the precision can be improved by extending the measurement time appropriately.

C. Dynamical phase calibration

In our experiments, we tune all qubits on the operating frequencies from their idle points with rectangular Z pulses after preparing the initial states. The total dynamical phase can be split into two parts. One comes from the difference between the idle frequency ω_{idle} and the target operating frequency ω_{targ}

$$
\Delta\phi_1 = (\omega_{\mathrm{targ}}-\omega_{\mathrm{idle}})t, \tag{S36}
$$

where t is the evolution time. The other results from the imperfect rectangle Z pulse (e.g. rising and falling edges, and distortions), which can be expressed as

$$
\Delta\phi_2 = \int_0^t \left[\omega_{\mathrm{actu}}(t)-\omega_{\mathrm{targ}}\right]\mathrm{d}t, \tag{S37}
$$

with $\omega_{\mathrm{actu}}(t)$ being the time-independent qubit frequency biased by the actual Z pulse. The total phase accumulation is thus given by $\Delta\phi = \Delta\phi_1 + \Delta\phi_2$.

For an experiment like quantum walks without phase measurement, the phase accumulation does not affect the expectations of observables such as the populations or probabilities. However, in the Loschmidt echo measurement, we need to compensate for phase accumulation to obtain the correct Pauli expectations $\langle\hat{\sigma}^x(t)\rangle$ and $\langle\hat{\sigma}^y(t)\rangle$, which represents the phase (off-diagonal) information of the qubit. We perform a Ramsey-like experiment to measure the phase accumulation via scanning the phase of the second $\pi/2$ pulse. The pulse sequence is shown in Fig. S8(a). For experiments without tuning couplings, we just apply the rectangular Z pulse on the qubit, while a periodic driving on the Z control line is added for the experiments that require tunable couplings. Compared with the experimental data before compensation (Fig. S8(b)), the phase accumulation can be almost completely compensated by adding the corresponding phase $\Delta\phi$, as seen in Fig. S8(c).

Note that the above experimental compensation is carried out in the frequency reference frame of the qubit itself. In the experimental data processing, one may consider the frame of reference frequency ω_{ref} and multiply the measured off-diagonal observable $\langle\hat{\sigma}^+(t)\rangle = \langle\hat{\sigma}^x(t)\rangle + \mathrm{i}\langle\hat{\sigma}^y(t)\rangle$ by an additional phase factor $\exp(-\mathrm{i}\Delta\omega_{\mathrm{ref}}t)$ with $\Delta\omega_{\mathrm{ref}} = \omega_{\mathrm{ref}} - \omega_{\mathrm{targ}}$. Hence, the Fourier results are convoluted with $\delta(\omega - \Delta\omega_{\mathrm{ref}})$, and the corresponding energy spectrum will be shifted to the reference frame of ω_{ref}. As shown in Fig. S6(c), the shifted experimental results agree with the simulation results that minus the reference frequency. In fact, the shift simply depends on the chosen reference frequency and the relative values of the eigenenergies remain the same.
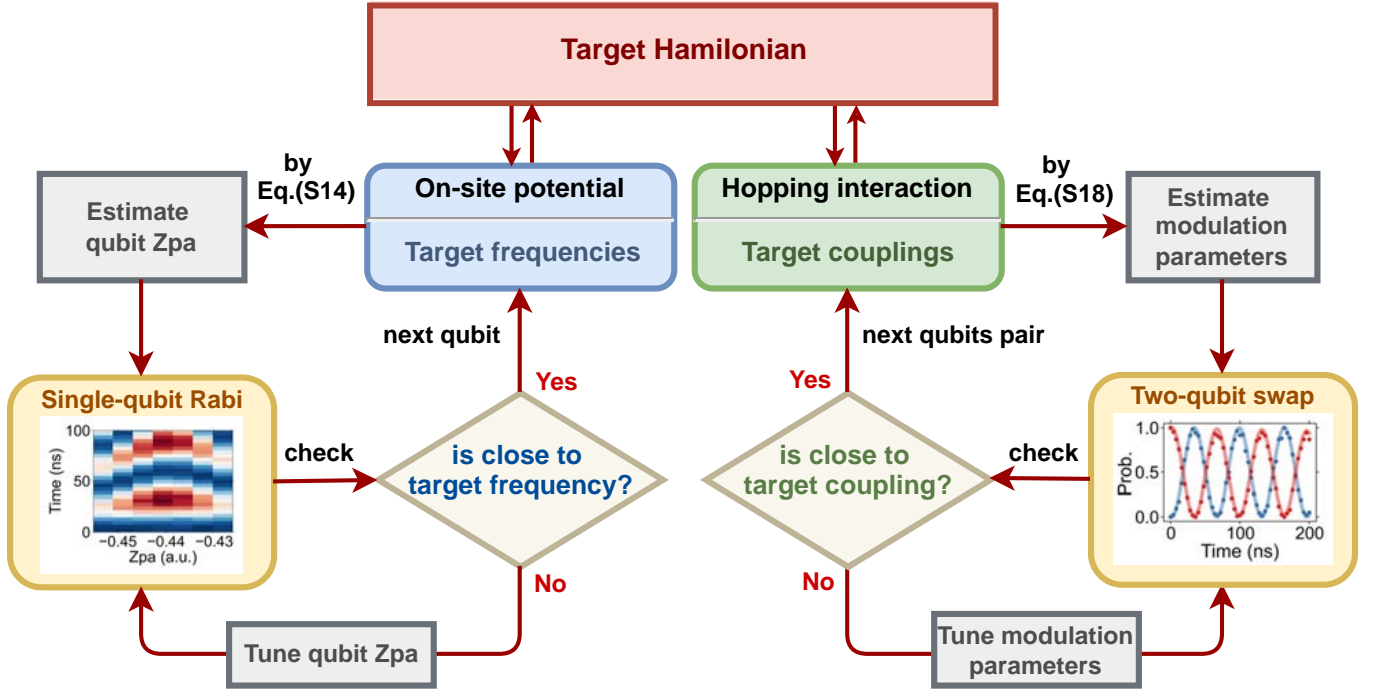
FIG. S9. Automatic calibration for the general quantum simulation schemes assisted by the Floquet engineering in superconducting circuits.

V. AUTOMATIC CALIBRATION SCHEME

In this section, we will give a brief introduction to the automatic calibration scheme for the general quantum simulation tasks assisted by Floquet engineering in superconducting circuits. The whole calibration diagram is briefly shown in Fig. S9.

For a general quantum simulation task, the core is to construct the target Hamiltonian. In most superconducting circuits, the total Hamiltonian can be split into two terms, namely the on-site potential (target frequencies) and the hopping interaction (target couplings). Our aim is to engineer these two parts. For the on-site potential, we apply the rectangular Z pulse on the qubit, and its frequency can be controlled by the amplitude (Zpa) of this fast bias. For the hopping interaction, we apply the external periodic driving on the qubits Z line to adjust the neighboring couplings within a certain range. As mentioned in Sec. III, the hopping strength corresponds to the amplitude and frequency of the periodic driving.

After measuring the individual spectroscopic and Floquet parameters of each qubit, we obtain a rough mapping between the experimental parameters and the target Hamiltonian. However, to simulate the target Hamiltonian with high accuracy, we cannot directly use the parameters from the individual measurement to simultaneously manipulate the qubits. Because the crosstalk and complex interactions in multi-qubit quantum devices will lead to the deviation of experimental control parameters. Therefore, it is necessary to tune these parameters under synchronous control. In our experiments, we set this synchronous control environment for the frequencies of all non-target qubits being staggered approximately ± 80 MHz around the reference frequency ω_{ref}. In this environment, we sequentially calibrate the control parameters for each qubit or pair of qubits. The qubit frequency is measured by the vacuum Rabi oscillation and the coupling is characterized by the two-qubit swap experiment.

To simulate the diagonal AAH model, the hopping strength is fixed to about 7.6 MHz. For each b_v, we calibrate the frequencies to satisfy $\omega_j = \omega_{\mathrm{ref}} + v \cos(2\pi b_v j)$, with $v/(2\pi) = 15.2$ MHz and $\omega_{\mathrm{ref}}/(2\pi) \approx 5.107$ GHz. For the realization of the off-diagonal AAH model, the qubit frequencies are set as $\omega_j/(2\pi) = \omega_{\mathrm{ref}}/(2\pi) \approx 5.02$ GHz, and the couplings obey $g_j = u\left[1 + \lambda \cos(2\pi b_\lambda j + \varphi_\lambda)\right]$ with $\omega_{\mathrm{ref}}/(2\pi) \approx 5.02$ GHz. We calibrate $u/(2\pi) = 4.78$ MHz and $\lambda = 0.4$ for $b_\lambda = 1/2$, while for $b_\lambda = 1/4$ we adjust $u/(2\pi) = 3.35$ MHz, with $\lambda = 1.0$ and $u/(2\pi) = 2.77$ MHz, with $\lambda = \sqrt{2}$.

Note that the Hamiltonian parameters used in the numerical simulation have not been adjusted to fit the experimental results. Once the experimental control parameters, corresponding to the frequencies and couplings of the target Hamiltonian, were calibrated, we built experimental circuits and performed measurements. It is also important that in the energy spectrum measurement, the calibration of the dynamical phase is required; otherwise, the measured spectrum data will have an overall shift relative to the numerical simulation data. Therefore, we must eliminate the accumulation of the dynamical phase by inserting a virtual Z gate before the experimental measurement, see Sec. IV.
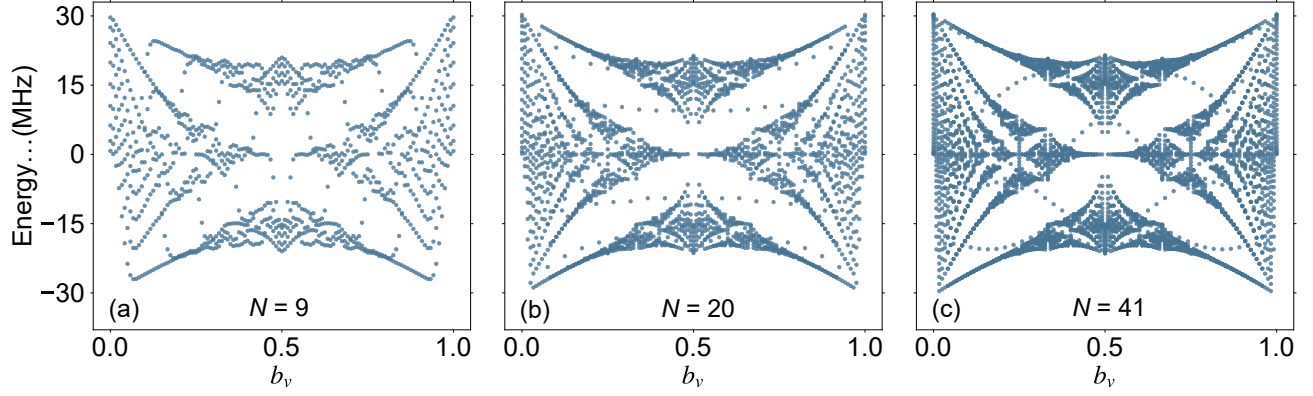
FIG. S10. Finite-size effects on the Hofstadter butterfly energy spectrum of diagonal AAH models with $u/(2\pi) = 7.6$ MHz and $v = 2u$.

VI. ADDITIONAL DISCUSSION

In Figs. S10–S12, we show numerical results for the band structures of generalized AAH models with different numbers of qubits. The clear and rich features in the band structures are attributed to the sufficiently large qubit number of our quantum processor. For instance, the fractal structure of Hofstadter butterfly spectrum is very unclear by using 9 qubits. Even with 20 qubits, this band structure cannot be captured clearly, and moreover, these results are just ideal numerical simulations. Furthermore, our work experimentally simulates topological phases on a NISQ device when the noise and decoherence cannot be ignored. The exact numerical simulation of the effects of decoherence is beyond the capability of a classical supercomputer.

In the generalized AAH model, the particle-hole symmetry is usually protected, contributing to the stability of the edge modes [1, 9]. However, the existence of weak next-nearest-neighboring hopping of our sample slightly breaks the particle-hole symmetry. In our sample, this NNN hopping is site-dependent and disordered. The corresponding Hamiltonian is $\hat{H}_{\mathrm{NNN}} = \sum_{j=1}^{N-2} g_{j,j+2}\hat{a}_j^\dagger \hat{a}_{j+2} + \mathrm{H.c.}$, where the average of $g_{j,j+2}/(2\pi)$ is about 0.7 MHz (standard deviation 0.3 MHz). In Fig. S13, we compare the experimental results with the theoretical results with and without NNN couplings in the commensurate off-diagonal AAH models with $b_\lambda = 1/2$. The topological edge modes (highlighted in red) have a small shift of the zero energy due to the existence of weak NNN couplings. However, the experimental results still show the robustness of the topological zero-energy edge states in the commensurate off-diagonal AAH models. For the generic commensurate off-diagonal AAH models with $b_\lambda = 1/4$, the NNN coupling opens a gap between the two central bands, leading to the shift of the topological zero-energy edge states to mid-gap edges, as shown in Fig. S14. This also verifies the robustness of the topological properties of the generic commensurate off-diagonal AAH model.

---

[1] S. Ganeshan, K. Sun, and S. Das Sarma, Topological zero-energy modes in gapless commensurate Aubry-André-Harper models, Physical Review Letters **110**, 180403 (2013).

[2] Y. E. Kraus, Y. Lahini, Z. Ringel, M. Verbin, and O. Zilberberg, Topological states and adiabatic pumping in quasicrystals, Physical Review Letters **109**, 106402 (2012).

[3] I. I. Satija and G. G. Naumis, Chern and Majorana modes of quasiperiodic systems, Physical Review B **88**, 1 (2013).

[4] W. Degottardi, D. Sen, and S. Vishveshwara, Majorana fermions in superconducting 1D systems having periodic, quasiperiodic, and disordered potentials, Physical Review Letters **110**, 1 (2013).

[5] Z. Chen, A. Megrant, J. Kelly, R. Barends, J. Bochmann, Y. Chen, B. Chiaro, A. Dunsworth, E. Jeffrey, J. Y. Mutus, P. J. O'Malley, C. Neill, P. Roushan, D. Sank, A. Vainsencher, J. Wenner, T. C. White, A. N. Cleland, and J. M. Martinis, Fabrication and characterization of aluminum airbridges for superconducting microwave circuits, Applied Physics Letters **104**, 052602 (2014).

[6] W. Cai, J. Han, F. Mei, Y. Xu, Y. Ma, X. Li, H. Wang, Y. P. Song, Z.-Y. Xue, Z.-q. Yin, S. Jia, and L. Sun, Observation of topological magnon insulator states in a superconducting circuit, Physical Review Letters **123**, 080501 (2019).

[7] S. K. Zhao, Z.-Y. Ge, Z. Xiang, G. M. Xue, H. S. Yan, Z. T. Wang, Z. Wang, H. K. Xu, F. F. Su, Z. H. Yang, H. Zhang, Y.-R. Zhang, X.-Y. Guo, K. Xu, Y. Tian, H. F. Yu, D. N. Zheng, H. Fan, and S. P. Zhao, Probing operator spreading via Floquet engineering in a superconducting circuit, Physical Review Letters **129**, 160602 (2022).

[8] J. Koch, T. M. Yu, J. Gambetta, A. A. Houck, D. I. Schuster, J. Majer, A. Blais, M. H. Devoret, S. M. Girvin, and R. J. Schoelkopf, Charge-insensitive qubit design derived from the Cooper pair box, Physical Review A **76**, 042319 (2007).

[9] S. Ryu and Y. Hatsugai, Topological origin of zero-energy edge states in particle-hole symmetric systems, Physical Review Letters **89**, 077002 (2002).
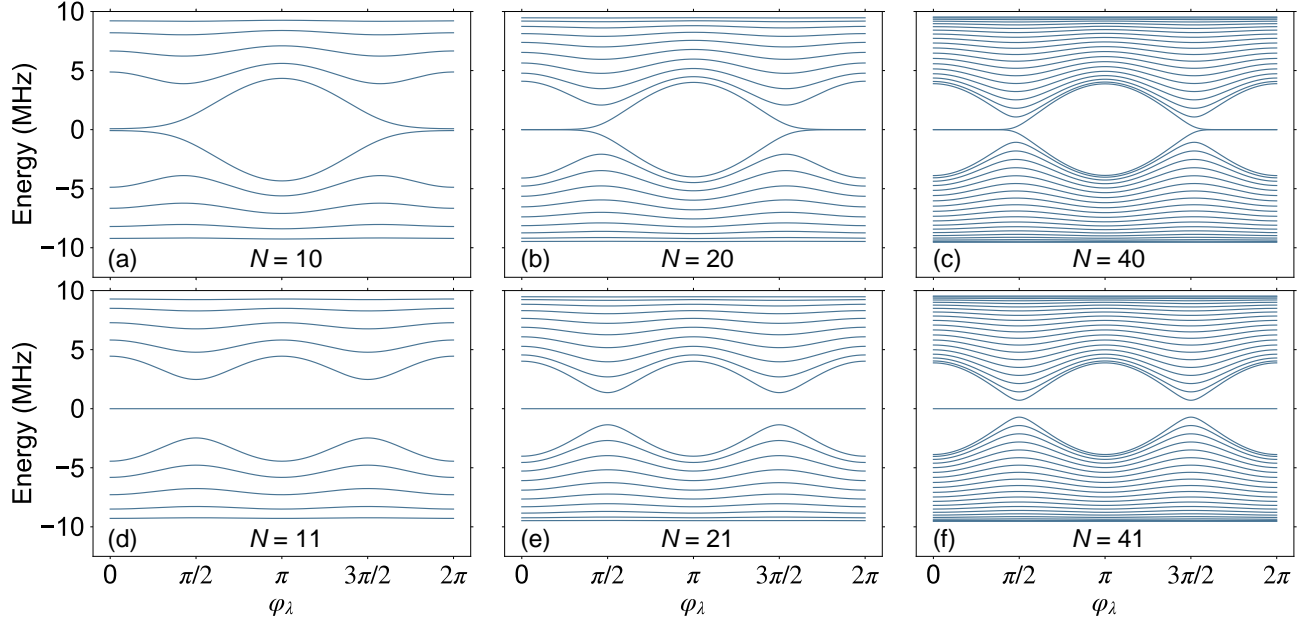

FIG. S11. Finite-size effects on the energy spectrum of commensurate off-diagonal AAH models for π-flux ($b_\lambda = 1/2$). Here we set $u/(2\pi) = 4.78$ MHz and $\lambda = 0.4$.
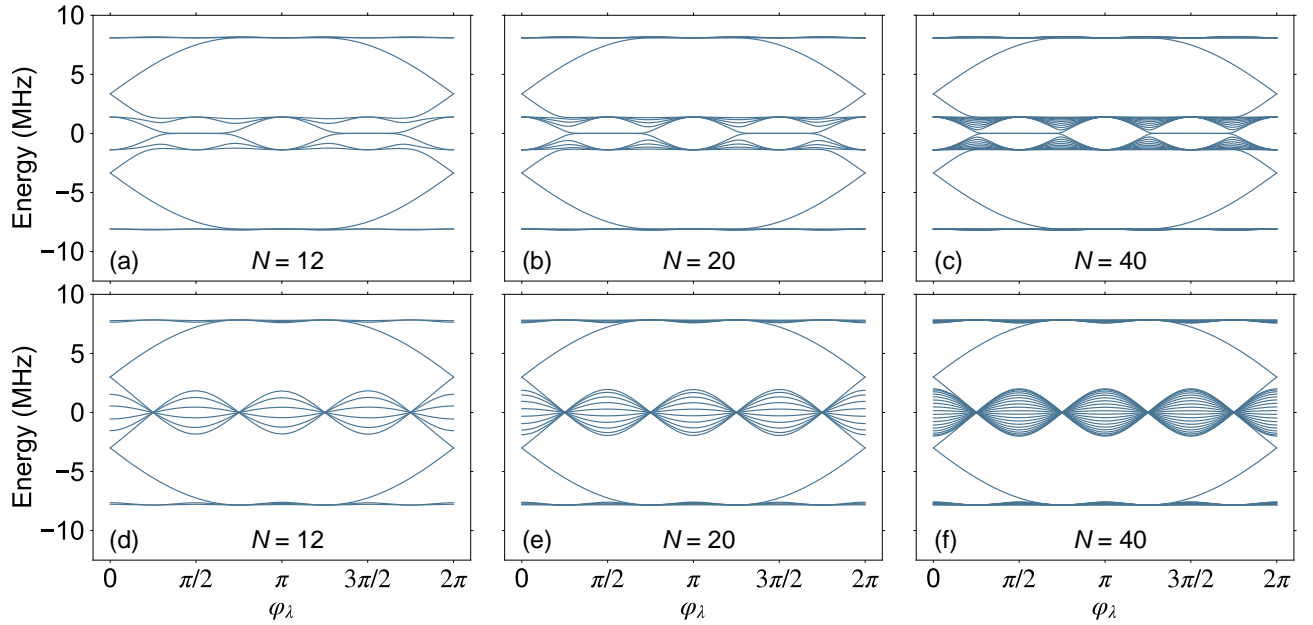

FIG. S12. Finite-size effects on the energy spectrum of generic commensurate off-diagonal AAH models with $b_\lambda = 1/4$. (a)-(c), Band structure for $\lambda = 1$ and $u/(2\pi) = 3.35$ MHz. (d)-(e), Band structure for $\lambda = \sqrt{2}$ and $u/(2\pi) = 2.77$ MHz.
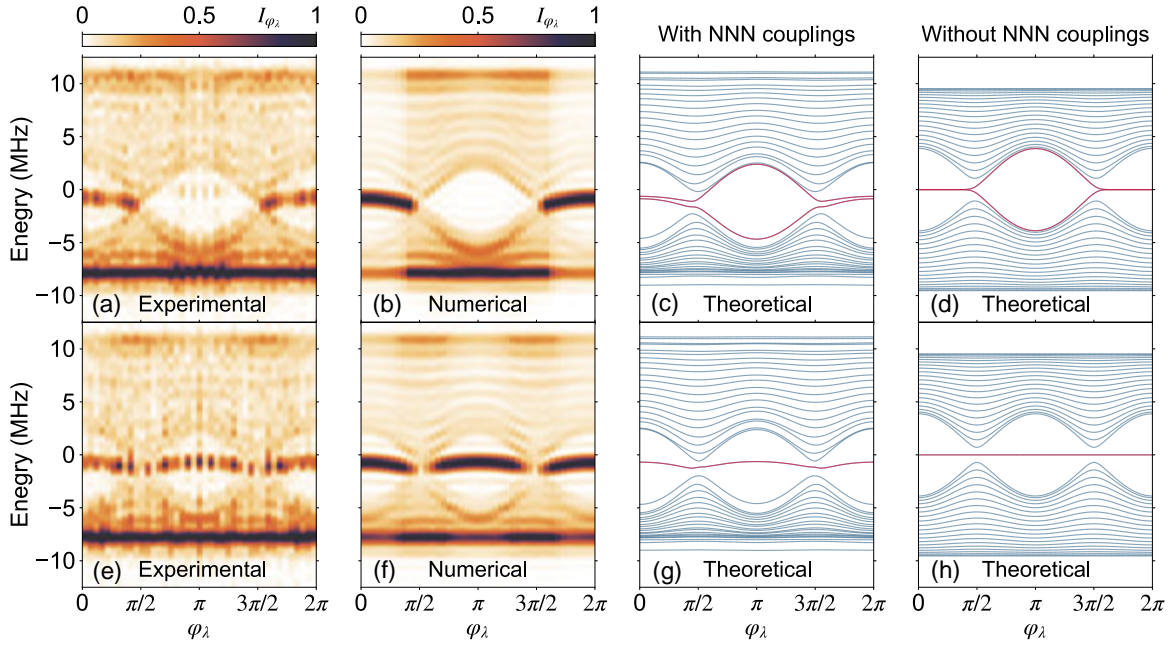
FIG. S13. Topological zero-energy edge modes in commensurate off-diagonal AAH models for π-flux ($b_\lambda = 1/2$). (a)-(e) Band structure spectroscopy of off-diagonal AAH models with even number $N = 40$ (a-d) and odd number $N = 41$ (e)-(h) of sites. Here we set $u/(2\pi) = 4.78$ MHz and $\lambda = 0.4$. (a) and (e), Experimental data for I_{φ_λ}. (b) and (f), Numerical data for I_{φ_λ} considering NNN couplings. (c) and (g), Theoretical eigenenergy spectrum with NNN couplings. (d) and (h), Theoretical eigenenergy spectrum without NNN couplings. The topological edge modes (highlighted in red) are verified to be robust, although the energies are slightly shifted away from zero.
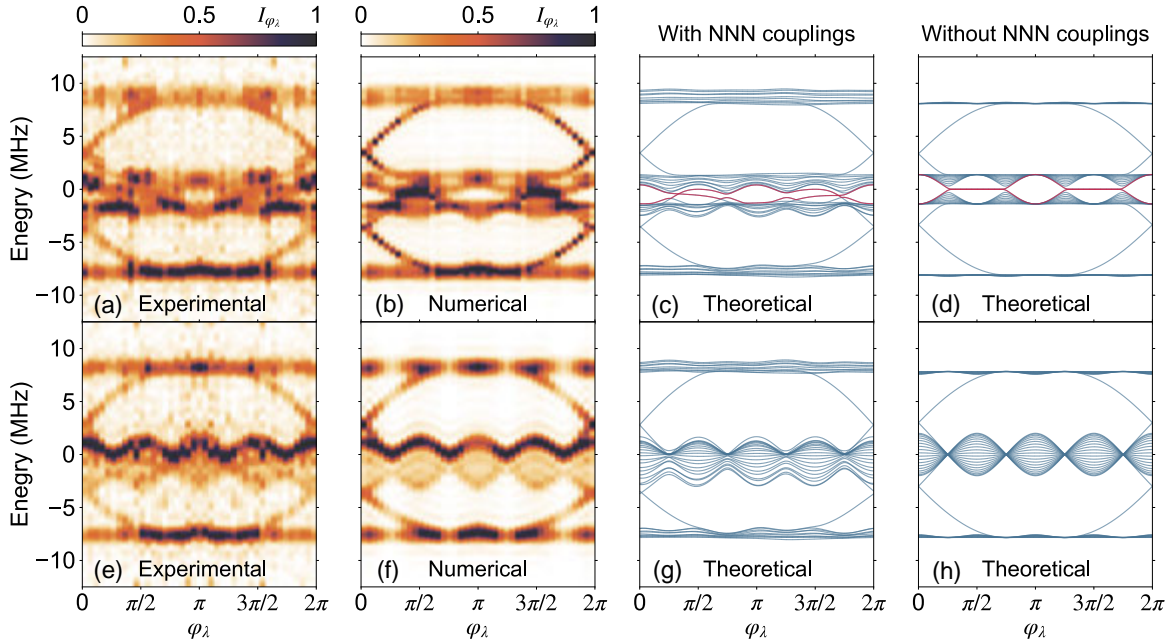

FIG. S14. Band structure spectroscopy of generic commensurate off-diagonal AAH models with $N = 40$ sites for $b_\lambda = 1/4$. (a)-(d), Band structure for $\lambda = 1$ and $u/(2\pi) = 3.35$ MHz. The gap between two central bands opens near $\varphi_\lambda = 0$ and π. The topologically nontrivial zero-energy modes are observed between two central bands. (e)-(h), Band structure for $\lambda = \sqrt{2}$ and $u/(2\pi) = 2.77$ MHz. The gap between the two central bands closes, and no topological edge states between these two bands are observed. (a) and (e), Experimental data for I_{φ_λ}. (b) and (f), Numerical data for I_{φ_λ} considering NNN couplings. (c) and (g), Theoretical eigenenergy spectrum with NNN couplings. (d) and (h), Theoretical eigenenergy spectrum without NNN couplings.